metals

MDPI

Article

The Structure and Magnetic Properties of $Sm_2Fe_{17}C_x$ Compounds Prepared from Ball-Milled Mixtures of Sm_2Fe_{17} and Carbon Nanotubes or Graphite

Vladislav A. Mikheev, Igor G. Bordyuzhin, Mikhail V. Gorshenkov, Elena S. Savchenko, Irina V. Dorofievich and Igor V. Shchetinin *

Department of Physical Materials Science, National University of Science and Technology «MISIS», Leninsky Prospekt 4 Bld.1, Moscow 119049, Russia; vmikheev@misis.ru (V.A.M.); i.bordiuzhin@misis.ru (I.G.B.); mvg@misis.ru (M.V.G.); savchenko.es@misis.ru (E.S.S.)

* Correspondence: ingvar@misis.ru

Abstract: The processing route of Sm_2Fe_{17} carbides is shorter than that of nitrides, which can potentially be used for cost-effective mid-performance magnets' production. The magnetic properties of $Sm_2Fe_{17}C_x$ compounds can be controlled at the annealing step, which allows them to be used for a variety of applications. In this work, X-ray diffraction (XRD) analysis, Mössbauer spectroscopy, scanning and transmission electron microscopy (SEM, TEM) and vibrating sample magnetometry (VSM) were used for characterization of the structure and magnetic properties of $Sm_2Fe_{17}C_x$ compounds. The powder samples were prepared by high-energy ball milling of Sm_2Fe_{17} mixtures with carbon nanotubes (CNT) or graphite with subsequent annealing. The formation of $Sm_2Fe_{17}C_x$ compounds after annealing was followed by the formation of α-Fe and amorphous Sm_2O_3. The hyperfine field values of Fe atoms of all the Sm_2Fe_{17} lattice sites increased by 12% on average after annealing that was caused by carbon diffusion. The coercivity of the samples peaked after annealing at 375 °C. The samples with CNT demonstrated an increase of up to 14% in coercivity and 5% in specific remanence in the range of 250–375 °C annealing temperatures.

Keywords: Sm_2Fe_{17}; Sm_2Fe_{17} carbides; Sm-Fe-C; $Sm_2Fe_{17}C_x$; carbon nanotubes; high-energy ball milling; hard magnets; ferromagnetism; ternary carbide

Citation: Mikheev, V.A.; Bordyuzhin, I.G.; Gorshenkov, M.V.; Savchenko, E.S.; Dorofievich, I.V.; Shchetinin, I.V. The Structure and Magnetic Properties of $Sm_2Fe_{17}C_x$ Compounds Prepared from Ball-Milled Mixtures of Sm_2Fe_{17} and Carbon Nanotubes or Graphite. *Metals* **2024**, *14*, 472. https://doi.org/10.3390/met14040472

Academic Editor: Ian Baker

Received: 22 March 2024
Revised: 9 April 2024
Accepted: 16 April 2024
Published: 18 April 2024

1. Introduction

Modern trends in the development of alternative energy determine increased demand for rare earth permanent magnets implemented in generators and electric motors [1–7]. For permanent magnets used in direct-drive wind turbines, corrosion resistance is important, as the turbine is often located in high-humidity areas where the insulation of the generator is aging intensively [8]. Ferrite magnets' efficiency as a material for wind turbines was considered due to its low cost and corrosion resistance [9]. Recently, a soft magnetoelastic composite material was developed for wind-energy generation based on the giant magnetoelastic effect that could operate in water and withstand harsh conditions [10].

In this regard, the $Sm_2Fe_{17}N_x$ compound can also be considered as a hard magnetic material for wind generator systems. Originally, it was synthesized by J.M.D. Coey and Hong Sun in 1990 using heating in ammonia or nitrogen [11]. The Sm_2Fe_{17} cell is of the Th_2Zn_{17} type, where Sm atoms are located in 6c sites and Fe atoms are located in 6c, 9d, 18f and 18h sites. The easy magnetization direction lies in the basal plane in the whole temperature range. During nitrogenation, nitrogen atoms occupy 9e interstitial sites. This results in the Sm_2Fe_{17} lattice expansion. The magnetic anisotropy changes drastically after interstitial modification: the anisotropy transits from an easy-plane type to an easy-axis type, which determines the high magnetocrystalline constant of the $Sm_2Fe_{17}N_x$ compounds. Moreover, a growth in the Curie temperature up to 470 °C is observed [12].

As a result, the discovered Sm-Fe-N system promises great potential for hard magnetic applications provided with its higher Curie temperature and corrosion resistance than those of Nd-Fe-B [13–15]. Recent research has been dedicated to improvement of Sm-Fe-N powder properties and techniques of obtaining bonded magnets [16–19]. Currently, there is a gap between high-performance rare-earth magnets, which are expensive, and low-cost magnets without rare-earth elements, which have a low energy product. The development of a material with moderate magnetic properties and more affordable raw materials than those of Nd-Fe-B and Sm-Co would fill the mentioned gap. Another advantage of the Sm-Fe-N system is the relatively low content of expensive rare-earth elements. In total, 23.3 wt.% of Sm is needed for $Sm_2Fe_{17}N_3$ compared to 26.7 wt.% of Nd for $Nd_2Fe_{14}B$, provided with a lower cost of Sm with respect to Nd.

However, $Sm_2Fe_{17}N_x$ powder production includes the nitrogenation process of Sm_2Fe_{17}, which lasts for dozens of hours [20]. This time-consuming step can be excluded by replacing nitrogen with carbon, as similar structural effects were observed in $Sm_2Fe_{17}C_x$ [21–25].

There are different processing routes to synthesize the $Sm_2Fe_{17}C_x$ compound. The most common one is the ball milling of solid Sm, Fe or Sm-Fe mixtures with graphite [26,27]. Gas-phase carbonation has also been reported, where heat treatment in an acetylene (C_2H_2) atmosphere at about 500 °C for few hours was used [28]. A synthesis from the liquid was recently proposed where heptane (C_7H_{16}) was used as both the surfactant agent and the carbon source for the Sm-Fe alloy during milling [29].

Oxidation is a general problem for rare-earth-based compounds. The oxidation of Sm may occur during milling caused by a friction-induced local temperature rise which may be prevented by milling in liquid nitrogen [30]. Oxidation in the next step can be controlled by opening milling jars in a glovebox connected to the furnace directly [31]. Annealing is usually performed in vacuum furnaces; however, H_2 flow is also used [32]. An alternative technology is the reduction-diffusion process where Ca stands as a reductant for samarium oxide during heat treatment [33].

$Sm_2Fe_{17}C_x$ compounds tend to decompose when heated above 512 °C, which makes the conventional sintering technique by powder hot pressing above 1100 °C used for Sm_2Fe_{17} inappropriate [34]. To stabilize a 2:17 lattice, a substitution method was suggested where Fe was partially substituted with Ga which lifted the Curie temperature and decomposition temperature. This allowed the researchers to hot press, but the energy product of the compound was low (45 $kJ \cdot m^{-3}$), as non-magnetic Ga weakened the remanence [35,36]. Al substitution also improves Sm_2Fe_{17} carbide stability, as researchers have managed to synthesize single-phase $Sm_2Fe_{15}Al_2C_x$ compounds with an enhanced anisotropy field [37]. Higher Al substitution decreased the anisotropy of $Sm_2Fe_{13}Al_4C_x$, but the samples remained single-phase and showed an increased Curie temperature [38].

In this work, we investigated the influence of carbon modification on the structure formation and magnetic properties of $Sm_2Fe_{17}C_x$ compounds obtained by the high-energy ball milling of mixtures of Sm_2Fe_{17} and carbon nanotubes (CNT) or graphite with subsequent annealing.

2. Materials and Methods

2.1. Materials

The initial components were represented by an alloy of Sm-Fe in a system with 24 wt.% Sm content, multi-walled CNT and graphite. After homogenization, the Sm-Fe alloy was single-phase, containing the Sm_2Fe_{17} (R-3m) phase according to XRD analysis.

In total, 19.44 g of Sm_2Fe_{17} was mixed with 0.56 g of CNT or graphite so that the number of carbon atoms per formula unit of $Sm_2Fe_{17}C_x$ compound x was 3 (x = 3):

$$Sm_2Fe_{17} + 3C = Sm_2Fe_{17}C_3. \quad (1)$$

Then, the mixtures were milled in the 'Activator 2S' (Novosibirsk, Russia) planetary ball mill for 5 h at jar rotation speed of 400 rpm for 5 h in Ar (99.9999% pure). The jar volume was 250 mL. For the milling, steel balls of various diameter were used: 4 balls of 15 mm,

5 of 12 mm, 17 of 10 mm, 35 of 8 mm and 80 of 6 mm, so that the ball-to-powder mass ratio was 15:1. After milling, the powder was kept in a glovebox for 1 day for passivation. Annealing was carried out in a vacuum furnace for 1 h at the pressure of 1 Pa. The annealing temperature range was 250–450 °C. The heating rate was 15 K·min^{-1}. The samples cooled down with the furnace.

2.2. Characterization

X-ray diffraction analysis (XRD) was performed using a Rigaku MiniFlex diffractometer with CoK_α radiation in the 20–120° 2θ range. The powder was placed into flat cuvettes, moistened with ethanol and flattened with glass. The spectra were analyzed with the Rietveld method using PHAN% and SPECTRUM programs developed by the Physical Materials Science Department of MISIS University [39]. The diffraction lines broadening analysis was carried out by the Rietveld method and the parameters of the fine structure were determined: crystallite size (d) and microstrains (ε). Exclusion of the instrumental broadening was accomplished by using the LaB_6 standard.

XRD was used for both phase analysis and evaluation of the number of carbon atoms per formula unit of the $Sm_2Fe_{17}C_x$ phase. According to [26], the cell volume of the $Sm_2Fe_{17}C_x$ phase increased almost linearly in the range of x = 0–3. In current research, a linear approximation (R^2 = 0.975) of these data was used to calculate the actual x by measuring the cell volume V using XRD:

$$x = 60 \cdot V - 47.16. \quad (2)$$

where x is the number of carbon atoms per $Sm_2Fe_{17}C_x$ formula unit, V is the cell volume of the $Sm_2Fe_{17}C_x$ phase (nm^3).

Scanning electron microscopy (SEM) images were taken by using JEOL JSM-IT500 (Tokyo, Japan) and Tescan Vega 3SB (Czech Republic) microscopes for particle morphology investigation in secondary electron emission mode. Before scanning, the powders were dispersed in ethanol by using the ODA-LQ60 ultrasonic bath at a frequency of 40 kHz for 1 h. Then, the particle suspension was deposited on the surface of conductive carbon tape and then transferred to a silicon wafer.

Transmission electron microscopy (TEM) images were taken by using a JEOL JEM-1400 (Tokyo, Japan) microscope for particle structure investigation. Firstly, the sample was observed in bright-field mode until a distinct diffraction pattern was obtained. Then, one of the reflections was selected in diffraction mode. By doing this, the TEM was switched to dark-field mode where the bright contrast is formed by the equally oriented grains of the same phase that satisfy the Bragg condition. The grain size distribution was calculated using the ImageJ program by measuring the length of bright-contrasted grains in the vertical direction.

Magnetic properties were measured by using a VSM-250 (Changchun, China) vibrating sample magnetometer at room temperature in fields up to 1.6 MA/m. Paraffin was used to solidify the powder into a copper cylinder. Then, the cylinder was fastened to a vibrating rod between electromagnet poles.

Mössbauer spectra were measured with an MS-1104Em (Rostov-on-Don, Russia) spectrometer at room temperature using ^{57}Co source. Spectra were analyzed using the Univem MS program. The experimental spectra were calibrated relative to α-Fe.

3. Results and Discussions

After milling, the XRD patterns of powders were represented mostly by the Sm_2Fe_{17} phase (R-3m in hexagonal settings) with a small presence of the α-Fe (Im3m) phase, as shown in Figure 1a,c. The fine structure parameters of the Sm_2Fe_{17} phase changed to d = 12.4 ± 0.4 nm and ε = 0.37 ± 0.01% after milling (Table 1, before milling d > 200 nm, ε = 0.06%), which was caused by the accumulation of crystalline defects during milling. The accumulated plastic deformation can lead to the formation of α-Fe, since such an effect has been reported for the high-pressure torsion of $Sm_2Fe_{17}N_x$ alloys [40]. The cell volume

of $Sm_2Fe_{17}C_x$ in CNT and graphite mixtures was 0.7906 ± 0.0004 and 0.7914 ± 0.0007 nm^3, respectively, which corresponds to x = 0.2 ± 0.1 and 0.3 ± 0.1 according to Formula (2). Thus, the low solubility of carbon of both modifications was observed after milling.

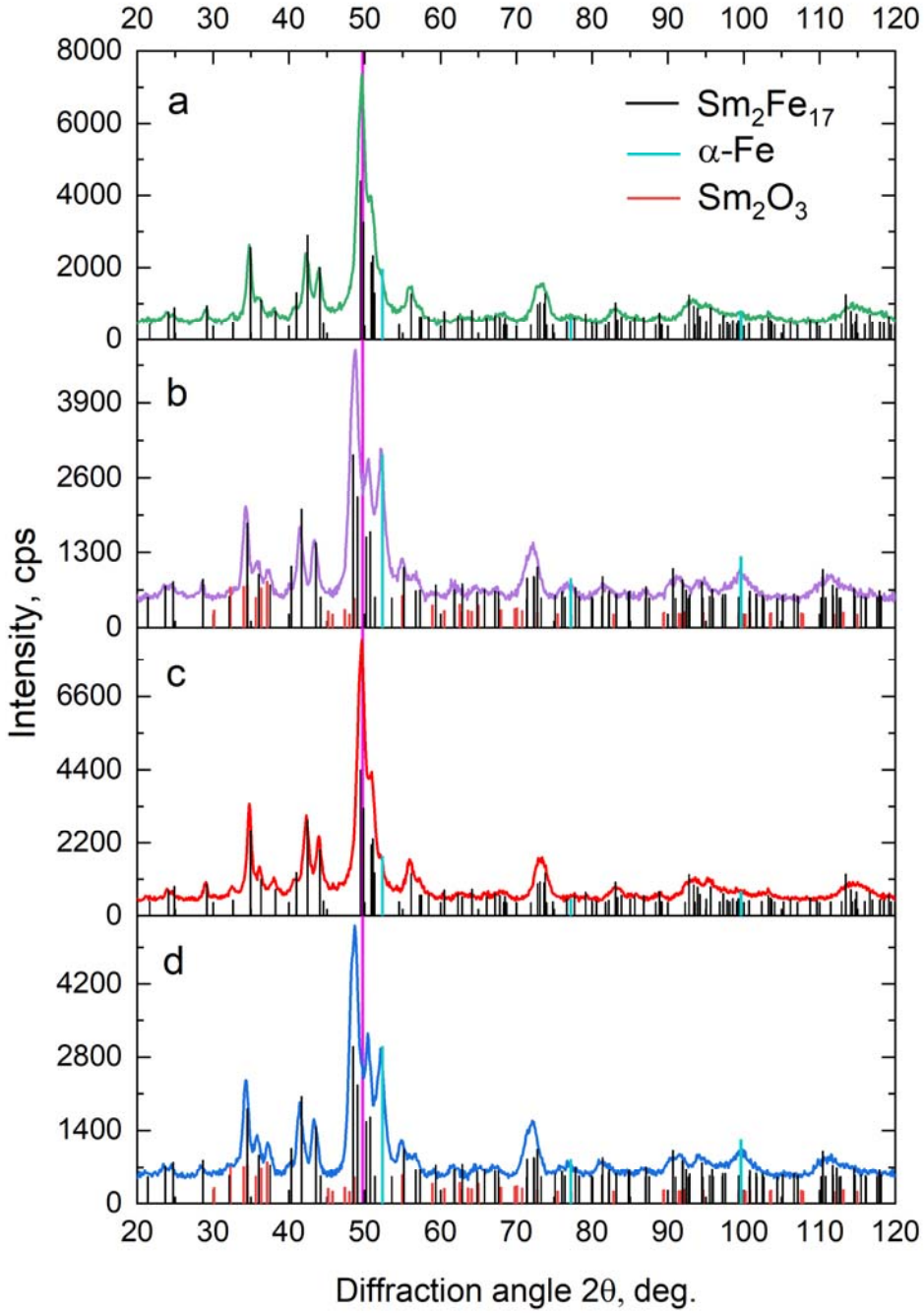

Figure 1. XRD patterns of mixtures of Sm_2Fe_{17} with: (**a**) carbon nanotubes (CNT) after milling, (**b**) CNT after milling and annealing (375 °C 1 h), (**c**) graphite after milling and (**d**) graphite after milling and annealing (375 °C 1 h).

Table 1. XRD measurement data of mixtures with carbon nanotubes (CNT) and graphite after milling (M) and annealing at 375 °C for 1 h (A).

Sample	Mass Fraction, %			$Sm_2Fe_{17}C_x$ Lattice Spacings, nm		$Sm_2Fe_{17}C_x$		α-Fe	
	$Sm_2Fe_{17}C_x$	α-Fe	Sm_2O_3	*a*	*c*	*d*, nm	*ε*, %	*d*, nm	*ε*, %
CNT M	93 ± 4	7 ± 1	–	0.8559 ± 0.0001	1.2460 ± 0.0003	12.4 ± 0.4	0.37 ± 0.01	9.0 ± 0.4	0.11 ± 0.07
CNT M+A	70 ± 3	24 ± 2	6 ± 1	0.8730 ± 0.0002	1.2556 ± 0.0004	15.4 ± 0.5	0.42 ± 0.02	8.3 ± 0.4	0.29 ± 0.03
graphite M	92 ± 4	8 ± 1	–	0.8565 ± 0.0002	1.2458 ± 0.0005	16.8 ± 0.5	0.44 ± 0.01	12.4 ± 0.4	0.09 ± 0.09
graphite M+A	72 ± 3	22 ± 1	6 ± 1	0.8720 ± 0.0001	1.2539 ± 0.0002	16.8 ± 0.5	0.44 ± 0.02	10.3 ± 0.4	0.48 ± 0.03

d: crystallite size parameter, *ε*: microstrain parameter.

According to SEM (Figure 2a,c), the milled powders consisted of particle agglomerates of 5–10 μm, which contained even smaller particles of less than 1 μm. The shape of the particles was close to uniaxial. The elemental analysis of the particles corresponds to the composition of the alloy before milling.

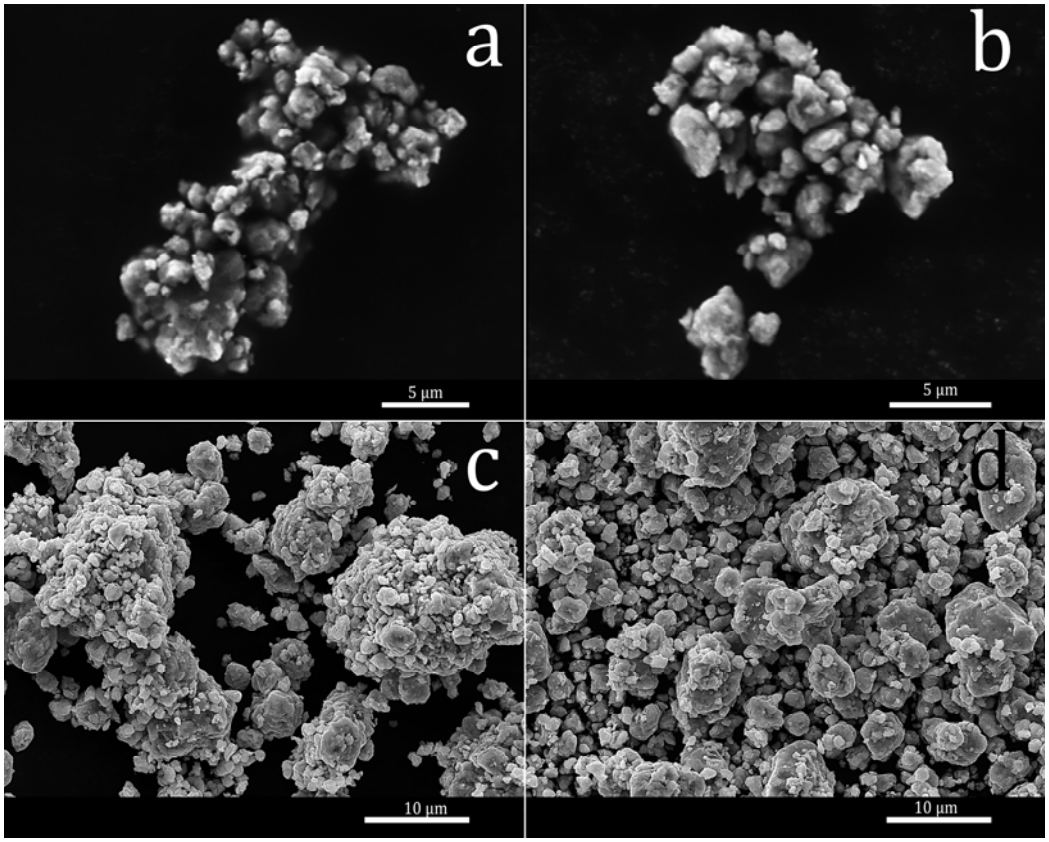

Figure 2. SEM images of mixtures (**a**) with CNT after milling (**b**) with CNT after milling and annealing (400 °C 1 h) (**c**) with graphite after milling and (**d**) with graphite after milling and annealing (375 °C 1 h).

The Mössbauer spectrum of the sample after milling (Figure 3a) was represented by a set of sextets, which indicates a magnetic order in the sample. The analysis of the spectrum showed that it could be described with a set of five sextets, the parameters of which are listed in Table 2. The first sextet in the Table 2 has an isomer shift value I_s of 0.00 mm/s and a hyperfine magnetic field value $\mu_0 H_{hf}$ of 33.0 T, which corresponds to the α-Fe phase. The relative area *S* of this sextet is well consistent with the phase analysis data (Table 1). The other four sextets correspond to four non-equivalent sites of Fe atoms in the $Sm_2Fe_{17}C_x$ phase: 6c, 9d, 18f and 18h. The values of the hyperfine field for each site are considered to depend on the number of iron and rare-earth neighbors of the site. In this model, the 6c site should have the largest hyperfine field since it is surrounded by the most iron and the

fewest rare-earth atoms [41]. Thus, the hyperfine field values in the series of 6c, 9d, 18f and 18h should decrease and they were well consistent with the data for pure Sm_2Fe_{17} [42,43]. This confirms the low solubility of carbon in the $Sm_2Fe_{17}C_x$ phase after milling proved by the XRD analysis, since the solubility of nitrogen or carbon in the Sm_2Fe_{17} phase should lead to noticeable enhancement of hyperfine magnetic field parameters [44]. The relative area of the corresponding sextets (Table 2) was also well consistent with the corresponding sites occupancies of iron atoms.

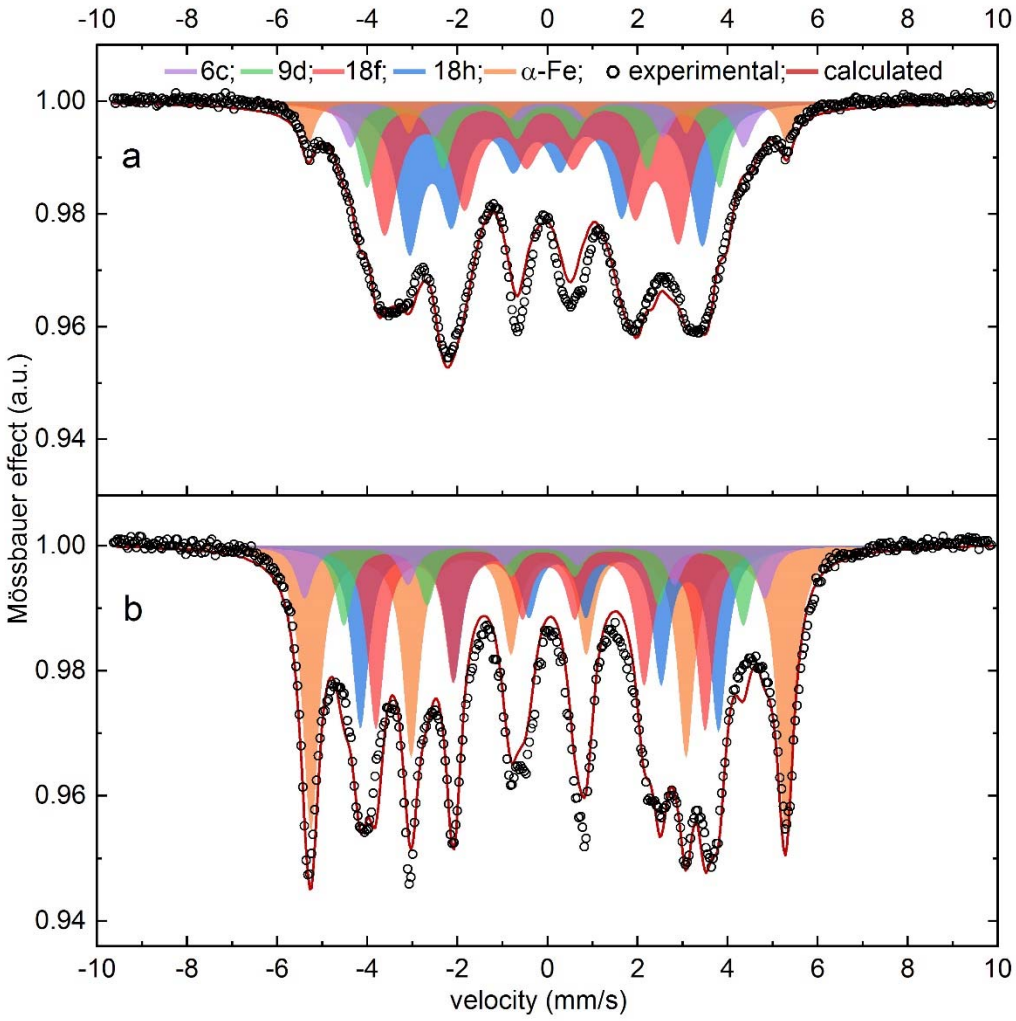

Figure 3. Mössbauer spectra of mixtures with CNT after: (**a**) milling, and (**b**) milling and annealing (375 °C 1 h).

Table 2. Mössbauer spectra parameters of mixtures with CNT after milling (M) and milling and annealing (375 °C 1 h) (M+A).

Sextet	I_s, mm/s		Q_s, mm/s		$\mu_0 H_{hf}$, T		S, %	
	M	M+A	M	M+A	M	M+A	I	M+A
α-Fe	0.00 ± 0.02	0.02 ± 0.02	0.00 ± 0.01	−0.01 ± 0.01	33.0 ± 0.5	32.7 ± 0.5	6 ± 1	39 ± 2
2:17 (6c)	0.01 ± 0.02	−0.21 ± 0.03	−0.05 ± 0.01	−0.15 ± 0.03	27.1 ± 0.5	31.7 ± 0.5	9 ± 1	6 ± 1
2:17 (9d)	−0.07 ± 0.02	−0.10 ± 0.02	−0.04 ± 0.01	0.02 ± 0.01	24.3 ± 0.5	27.5 ± 0.5	16 ± 1	7 ± 1
2:17 (18f)	−0.15 ± 0.03	0.02 ± 0.02	−0.41 ± 0.08	−0.40 ± 0.08	20.3 ± 0.5	24.7 ± 0.5	34 ± 2	25 ± 2
2:17 (18h)	−0.03 ± 0.02	−0.07 ± 0.02	0.43 ± 0.09	−0.18 ± 0.05	20.2 ± 0.5	22.7 ± 0.4	35 ± 2	23 ± 2

I_s: isomer shift, Q_s: quadrupole splitting, H_{hf}: hyperfine magnetic field, S: relative spectral area.

The magnetic properties measurements of the samples after milling showed low coercivity values of around 37 kA/m. This behavior was caused by the easy-plane magnetocrystalline anisotropy of the Sm_2Fe_{17} phase [45].

Since the number of carbon atoms per formula unit of the $Sm_2Fe_{17}C_x$ phase (x) was low after milling, the samples with CNT and graphite have been annealed in a vacuum for 1 h in the 250–450 °C annealing temperature range to stimulate the diffusion process. The phase diagram was plotted after the investigation of the phase composition of the powders (Figure 4). According to the diagram, the mass fraction of samarium oxide Sm_2O_3 (C2/m and amorphous) increases with the annealing temperature for both CNT and graphite-containing samples. This leads to α-Fe phase formation and must lead to the decrease in the coercivity of the samples. In the meantime, based on the cell volume measurements, the increase in the annealing temperature results in activation of the diffusion process and monotonic growth of x up to ≈2.7 (Figure 5). Such a significant increase in the number of carbon atoms per $Sm_2Fe_{17}C_x$ formula unit leads to a switch of magnetic anisotropy from an 'easy-plane' to an 'easy-axis' type [22] with the corresponding growth in the magnetocrystalline anisotropy constant [45]. As a consequence, this must result in an increase in coercivity. The obtained data are entirely confirmed by magnetic properties measurements (Figure 5, Table 3).

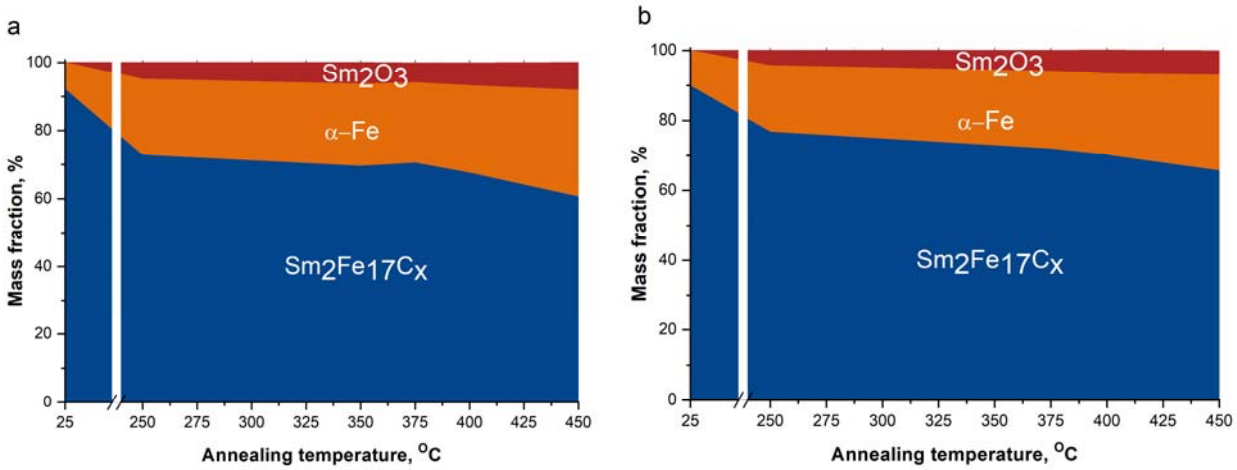

Figure 4. Phase composition of mixtures (**a**) with CNT and (**b**) with graphite.

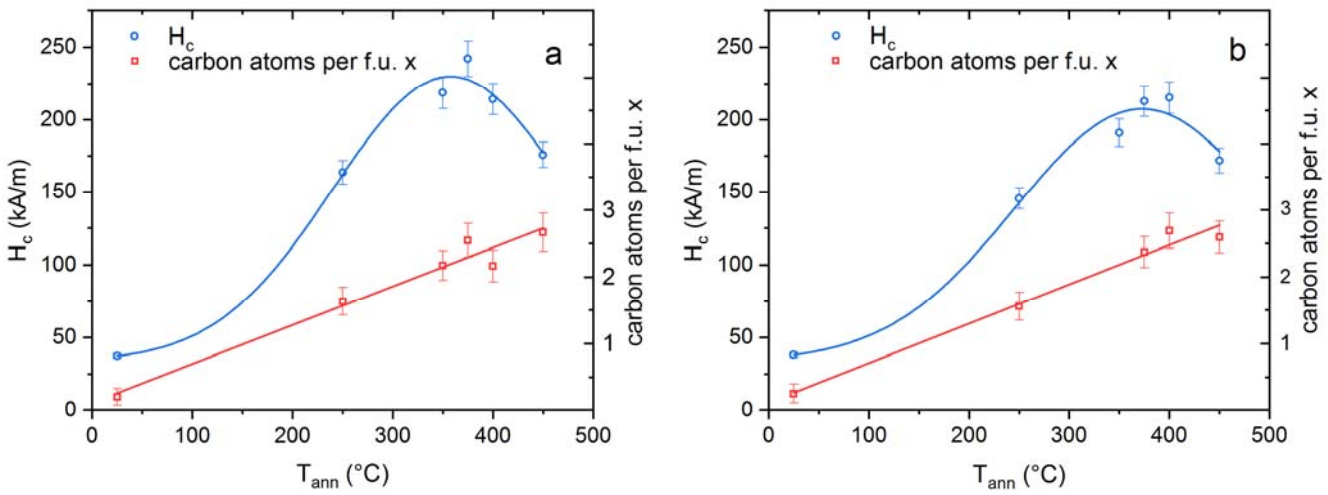

Figure 5. Carbon content and coercivity values of mixtures (**a**) with CNT and (**b**) with graphite.

Table 3. Magnetic properties of mixtures with CNT and graphite (G).

T_{ann}, °C	H_c, kA/m		σ_s, A·m²/kg		σ_r, A·m²/kg	
	CNT	G	CNT	G	CNT	G
25	37 ± 2	38 ± 2	103 ± 1	102 ± 1	18.7 ± 0.2	18.1 ± 0.2
250	164 ± 8	146 ± 7	104 ± 1	101 ± 1	38.3 ± 0.4	35.4 ± 0.4
350	219 ± 11	191 ± 10	101 ± 1	99 ± 1	40.5 ± 0.4	38.4 ± 0.4
375	242 ± 12	213 ± 11	99 ± 1	99 ± 1	42.6 ± 0.4	40.7 ± 0.4
400	214 ± 11	215 ± 11	100 ± 1	98 ± 1	38.5 ± 0.4	40.4 ± 0.4
450	176 ± 9	172 ± 9	100 ± 1	98 ± 1	36.2 ± 0.4	35.7 ± 0.4

T_{ann}: annealing temperature, H_c: coercivity, σ_s: specific saturation magnetization, σ_r: specific remanence.

The mass fraction of the $Sm_2Fe_{17}C_x$ phase consistently decreased with the rise in the annealing temperature (Figure 4), while the number of carbon atoms per formula unit of the $Sm_2Fe_{17}C_x$ phase (x) consistently increased (Figure 5). Consequently, the coercivity dependence from the annealing temperature had a maximum, at 375 °C. The mixtures with CNT and graphite showed a similar structure formation tendency, but the ones with CNT demonstrated 10–14% higher coercivity and 5% higher specific remanence in the 250–375 °C annealing temperature range (Table 3). A developed surface of CNT, supposedly, provides a larger mechanical contact area between carbon and metallic particles that contributes to faster diffusion of carbon in the case of relatively low annealing temperatures (250–375 °C) and limited time. The coercivity of the samples annealed at 400 °C did not depend on the carbon modification, since the temperature of annealing was sufficient for the process of carbon diffusion to complete within 1 h. Annealing above 400 °C also resulted in a complete carbon solution, but the active process of $Sm_2Fe_{17}C_x$ compound decomposition was triggered as well. This caused a significant coercivity drop for mixtures with both carbon additives.

Further investigations are presented for the samples annealed at 375 °C, since they showed the highest hysteresis properties.

After the annealing of CNT and graphite mixtures at 375 °C for 1 h, the cell volume of $Sm_2Fe_{17}C_x$ increased to 0.8286 ± 0.0007 and 0.8258 ± 0.0004 nm^3, respectively, which corresponds to the increase in the number of carbon atoms per $Sm_2Fe_{17}C_x$ formula unit up to x = 2.5 ± 0.3 and 2.4 ± 0.2. This is well observed by the shift of the highest peak of the Sm_2Fe_{17} with respect to the pink line (Figure 1). The increase in the lattice constants was caused by the diffusion of carbon into the Sm_2Fe_{17} phase during annealing provided with the formation of an interstitial solid solution. In the case of a substitutional solid solution, carbon would substitute samarium or iron atoms, which have larger atomic radii. As a result, the lattice constants would decrease. However, an opposite effect is observed experimentally, which confirms carbon to solubilize interstitially. Moreover, annealing triggered the formation of the α-Fe phase caused by the partial oxidation of samarium with the amorphous Sm_2O_3 phase formation. The similar process of α-Fe formation during post-pulverization annealing was reported in [46].

The decrease in the $Sm_2Fe_{17}C_x$ mass fraction caused by the formation of α-Fe and Sm_2O_3 implies excessive carbon presence in the mixtures that cannot be observed with XRD. However, the number of carbon atoms per formula unit of the carbide phase did not exceed $x > 2.7 \pm 0.3$. This could imply that maximum solubility of carbon for the Sm_2Fe_{17} alloy is around $x \sim 2.5$–3.0 atoms per cell unit, which is supported by other studies [26,34,35].

The specific saturation magnetization of annealed samples had a low correlation with the annealing temperature (Table 3). On the one hand, the formation of Sm_2O_3 and the increase in its mass fraction must reduce the specific saturation magnetization at higher annealing temperatures. On the other hand, the α-Fe mass fraction also increases, which must enhance the magnetization saturation. As a result, these two factors compensate each other so that a weak change in the values is observed. The peak of coercivity values is followed by specific remanence values that also demonstrate a maximum at a 375 °C annealing temperature for both types of mixtures. This maximum was also caused by

the superposition of both the mass fraction of the hard-magnetic $Sm_2Fe_{17}C_x$ phase and the number of carbon atoms per $Sm_2Fe_{17}C_x$ formula unit, which determines the level of anisotropy of that phase.

After annealing, the hyperfine field parameter values $\mu_0 H_{hf}$ (Table 2) of Fe atoms located in each of the $Sm_2Fe_{17}C_x$ lattice sites increased (by 12% on average), which indicates the change in the site surrounding (distances, neighbors) induced by the interstitial carbon presence. A similar effect was reported for the nitrogenation process of Sm_2Fe_{17}, where the 'nitrogen-poor' $Sm_2Fe_{17}N_x$ ($0 < x < 3$) phase had an average hyperfine field of ~24 T, considerably smaller than that of the 'fully nitride' $Sm_2Fe_{17}N_3$ phase of ~33 T [20]. The difference between the hyperfine field parameters of the Mössbauer spectra of the samples with carbon additives of both modifications did not exceed statistical error. According to [47,48], the formation of cementite Fe_3C phase is possible in similar systems. However, its presence was not confirmed by the Mössbauer spectra. Furthermore, the relative area S of the α-Fe sextet increased from 4% to 38% after annealing (Table 2). The relative area of the sextet is considered to be proportional to the corresponding lattice site occupancy. Therefore, the increase in the α-Fe sextet relative area correlates with the extra α-Fe formation observed with XRD.

According to SEM, the morphology and the size of the particles did not change considerably after annealing (Figure 2b,d), which correlates with the XRD average crystallite size analysis.

TEM imaging of the annealed powders demonstrated multi-phase particles consisting of α-Fe and $Sm_2Fe_{17}C_x$ grains (Figure 6). Since the most intense (110) spectral line of the α-Fe phase overlaps with the relatively highly intense (006) line of the $Sm_2Fe_{17}C_x$ phase, the reflexes of both phases are selected with a selected area aperture. Therefore, the bright contrast might be formed by both phases. The measured grain size was in the range of 4–17 nm, where, based on above considerations, the average size of 8 and 15 nm belonged to the α-Fe and $Sm_2Fe_{17}C_x$ phases, respectively. This also correlates with the average crystallite size values of the phases derived from XRD.

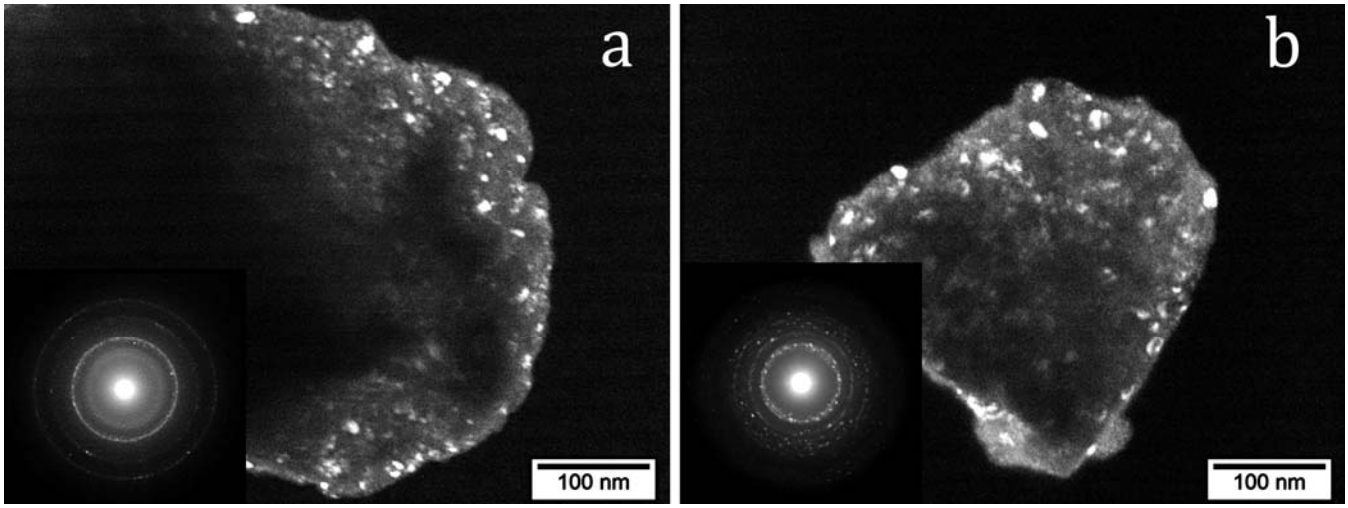

Figure 6. TEM dark-field images of annealed mixtures: (**a**) with CNT, (**b**) with graphite.

The magnetic properties of the $Sm_2Fe_{17}C_x$ compounds obtained in this study (Table 3) can be compared with those of strontium hexaferrite $SrFe_{12}O_{19}$ compounds. Under the same measurement conditions, strontium hexaferrites powder has a coercivity of 254 kA/m, which is quite close to that of the Sm-Fe samples with CNT annealed at 375 °C (considering statistical error). At the same time, $SrFe_{12}O_{19}$ powder has a specific saturation magnetization of 65 A·m^2/kg and a specific remanence of 33.5 A·m^2/kg [49]. These values are distinctly lower than those of the Sm-Fe samples with both CNT and graphite annealed at 375 °C. Consequently, the synthesized powder samples might potentially stand as a basis

for magnets that will fill the gap between strontium hexaferrites and high-performance rare-earth magnets.

Greater prospects for the $Sm_2Fe_{17}C_x$ compounds may be found in the field of biomedical applications, such as magnetic hyperthermia therapy. The ability to control the coercivity is essential for this type of treatment, since the thermal effect is observed only when the coercivity of the sample does not exceed the values of the external alternating magnetic field. For $SrFe_{12}O_{19}$ compounds, this is achieved by the substitution of Fe with In atoms, which gradually decreased the coercivity values of $SrFe_{12-x}In_xO_{19}$ (x = 0–1.7) [49]. In the similar way, the coercivity of ball-milled Sm_2Fe_{17} mixtures with CNT or graphite was controlled by the annealing temperature. In this work, the coercivity of the samples changed in the wide range of 37 ± 2 to 242 ± 12 kA/m. Therefore, a study of the hyperthermic effect of $Sm_2Fe_{17}C_x$ compounds can be an interesting topic for further investigations.

4. Conclusions

1. Mixtures of $Sm_2Fe_{17}C_x$ (x = 3) composition were obtained by mechanochemical synthesis with the addition of CNT or graphite. XRD analysis of the mixtures demonstrated the increase in the Sm_2Fe_{17} cell volume by 0.4% after milling with carbon additives that qualitatively indicated a carbon solution. However, quantitative analysis showed poor carbon solubility of x = (0.2 ± 0.1), regardless of the type of carbon modification.
2. Annealing after milling stimulated the diffusion process and caused an increase in the number of carbon atoms per $Sm_2Fe_{17}C_x$ formula unit. This reflected in the lattice constants' increase to the values of a = (0.8740 ± 0.0002) nm and c = (1.2563 ± 0.0004) nm after annealing at 400 °C, which corresponds to x = (2.69 ± 0.26). The maximum mass fraction of the $Sm_2Fe_{17}C_x$ phase was (79 ± 3)% for the mixture with CNT annealed at 250 °C for 1 h.
3. The solution of carbon into the Sm_2Fe_{17} phase enhanced hyperfine field values of all the Fe sites according to Mössbauer spectroscopy. The coercivity increased up to 10–14% when CNT were used compared to graphite in the 250–375 °C annealing temperature range. The maximum coercivity value of 242 kA/m was reached after annealing at 375 °C. Annealing above 400 °C induced the active decomposition of the $Sm_2Fe_{17}C_x$ compound, which resulted in a drop in hysteresis properties.

Author Contributions: Conceptualization, I.V.S.; methodology, I.G.B. and E.S.S.; validation, I.V.S.; formal analysis, V.A.M.; investigation, V.A.M., M.V.G. and I.V.D.; resources, I.G.B., M.V.G., I.V.D. and I.V.S.; data curation, V.A.M.; writing—original draft preparation, V.A.M., E.S.S., M.V.G. and I.V.D.; writing—review and editing, V.A.M., I.G.B. and I.V.S.; visualization, V.A.M. and I.V.S.; supervision, I.V.S.; project administration, I.V.S.; funding acquisition, I.V.S. All authors have read and agreed to the published version of the manuscript.

Funding: This research was funded by Russian Science Foundation (RSF), grant number 23-73-00114.

Data Availability Statement: The data presented in this study are available in article.

Conflicts of Interest: The authors declare no conflicts of interest.

References

1. Lacal-Arántegui, R. Globalization in the Wind Energy Industry: Contribution and Economic Impact of European Companies. *Renew. Energy* **2019**, *134*, 612–628. [CrossRef]
2. Boadu, S.; Otoo, E. A Comprehensive Review on Wind Energy in Africa: Challenges, Benefits and Recommendations. *Renew. Sustain. Energy Rev.* **2024**, *191*, 114035. [CrossRef]
3. Coey, J.M.D. Perspective and Prospects for Rare Earth Permanent Magnets. *Engineering* **2020**, *6*, 119–131. [CrossRef]
4. Namahoro, J.P.; Wu, Q.; Su, H. Wind Energy, Industrial-Economic Development and CO_2 Emissions Nexus: Do Droughts Matter? *Energy* **2023**, *278*, 127869. [CrossRef]
5. Summerfield-Ryan, O.; Park, S. The Power of Wind: The Global Wind Energy Industry's Successes and Failures. *Ecol. Econ.* **2023**, *210*, 107841. [CrossRef]
6. Yossri, W.; Ben Ayed, S.; Abdelkefi, A. Evaluation of the Efficiency of Bioinspired Blade Designs for Low-Speed Small-Scale Wind Turbines with the Presence of Inflow Turbulence Effects. *Energy* **2023**, *273*, 127210. [CrossRef]

7. Liu, F.; Wang, X.; Sun, F.; Kleidon, A. Potential Impact of Global Stilling on Wind Energy Production in China. *Energy* **2023**, *263*, 125727. [CrossRef]
8. Liu, Q.; Liu, X.; Li, Y.; Wang, M.; Chen, H.; Zhao, Y.; Ma, Y. Evaluation Method of Stator Insulation for Direct-Drive Wind Turbine Generator Based on Accelerated Multi-Factor Aging. In Proceedings of the 2019 IEEE Conference on Electrical Insulation and Dielectric Phenomena (CEIDP), Richland, WA, USA, 20–23 October 2019; pp. 138–141. [CrossRef]
9. Depraiter, L.; Goutte, S. The Role and Challenges of Rare Earths in the Energy Transition. *Resour. Policy* **2023**, *86*, 104137. [CrossRef]
10. Zhao, X.; Nashalian, A.; Ock, I.W.; Popoli, S.; Xu, J.; Yin, J.; Tat, T.; Libanori, A.; Chen, G.; Zhou, Y.; et al. A Soft Magnetoelastic Generator for Wind-Energy Harvesting. *Adv. Mater.* **2022**, *34*, 2204238. [CrossRef]
11. Coey, J.M.D.; Sun, H. Improved Magnetic Properties by Treatment of Iron-Based Rare Earth Intermetallic Compounds in Anmonia. *J. Magn. Magn. Mater.* **1990**, *87*, L251–L254. [CrossRef]
12. Capehart, T.W.; Mishra, R.K.; Pinkerton, F.E. $Sm_2Fe_{17}N_x$: Site and Valence of the Interstitial Nitrogen. *Appl. Phys. Lett.* **1991**, *58*, 1395–1397. [CrossRef]
13. Hadjipanayis, G.C. Nanophase Hard Magnets. *J. Magn. Magn. Mater.* **1999**, *200*, 373–391. [CrossRef]
14. Katter, M.; Wecker, J.; Kuhrt, C.; Schultz, L.; Grössinger, R. Magnetic Properties and Thermal Stability of $Sm_2Fe_{17}N_x$ with Intermediate Nitrogen Concentrations. *J. Magn. Magn. Mater.* **1992**, *117*, 419–427. [CrossRef]
15. Li, X.T.; Liu, W.Q.; Yue, M.; Li, X.L.; Yi, X.F.; Huang, X.L.; Zhang, D.T.; Chen, J.W. Corrosion Evaluation for Recycled Nd-Fe-B Sintered Magnets. *J. Alloys Compd.* **2017**, *699*, 713–717. [CrossRef]
16. Koo, K.; Kwon, Y.-T.; Park, J.Y.; Choa, Y.-H. Advanced Magnetic Actuation: Harnessing the Dynamics of $Sm_2Fe_{17-X}Cu_xN_3$ Composites. *ACS Appl. Mater. Interfaces* **2024**, *16*, 11872–11879. [CrossRef] [PubMed]
17. Coey, J.M.D.; Iriyama, T. Chapter 09—Bonded Sm-Fe-N Permanent Magnets. In *Woodhead Publishing Series in Electronic and Optical Materials*; Croat, J., Ormerod, J., Eds.; Woodhead Publishing: Sawston, UK, 2022; pp. 305–342. [CrossRef]
18. Takagi, K.; Hirayama, Y.; Okada, S.; Yamaguchi, W.; Ozaki, K. Novel Powder Processing Technologies for Production of Rare-Earth Permanent Magnets. *Sci. Technol. Adv. Mater.* **2021**, *22*, 150–159. [CrossRef] [PubMed]
19. Takagi, K.; Hirayama, Y.; Okada, S.; Hosokawa, A.; Yamaguchi, W. Recent Research Trend in Powder Process Technology for High-Performance Rare-Earth Permanent Magnets. *KONA Powder Part. J.* **2023**, *40*, 74–93. [CrossRef]
20. Takahashi, J.; Mitsui, Y.; Onoue, M.; Kobayashi, R.; Koyama, K. Nitridation Kinetics of Sm_2Fe_{17} Probed Using Mössbauer Spectroscopy. *J. Magn. Magn. Mater.* **2022**, *554*, 169295. [CrossRef]
21. Zhong, X.-P.; Radwański, R.J.; de Boer, F.R.; Jacobs, T.H.; Buschow, K.H.J. Magnetic and Crystallographic Characteristics of Rare-Earth Ternary Carbides Derived from R_2Fe_{17} Compounds. *J. Magn. Magn. Mater.* **1990**, *86*, 333–340. [CrossRef]
22. Kou, X.C.; Grössinger, R.; Jacobs, T.H.; Buschow, K.H.J. Magnetocrystalline Anisotropy and Magnetic Phase Transition in $R_2Fe_{17}C_x$-Based Alloys. *J. Magn. Magn. Mater.* **1990**, *88*, 1–6. [CrossRef]
23. Helmholdt, R.B.; Buschow, K.H.J. Crystallographic and Magnetic Structure of Ternary Carbides of the Type $Nd_2Fe_{17}C_x$. *J. Less-Common Met.* **1989**, *155*, 15–21. [CrossRef]
24. Zeng, Z.; Zheng, Q.; Lai, W.; Pan, C.Y. Electronic Structure and Magnetic Properties of $R_2Fe_{17}N_x$ (X=0,3,4) and $R_2Fe_{17}C_x$ (X=0,3), (R=Sm,Nd). *J. Appl. Phys.* **1993**, *73*, 6916–6918. [CrossRef]
25. Fersi, R.; Mliki, N.; Bessais, L. Influence of Chemical Substitution and Light Element Insertion on the Magnetic Properties of Nanocrystalline Pr_2Co_7 Compound. *Magnetochemistry* **2022**, *8*, 20. [CrossRef]
26. Mao, O.; Ström-Olsen, J.O.; Altounian, Z.; Yang, J. Characteristics of $Sm_2Fe_{17}C_x$ Compounds Prepared from Ball-milled Blends of Sm_2Fe_{17} and Graphite. *J. Appl. Phys.* **1996**, *79*, 4619–4621. [CrossRef]
27. Geng, D.; Zhang, Z.; Cui, B.; Zhao, X.; Liu, W.; Guo, Z. Sm–Fe–C Nanocomposite Magnets Prepared from Powders of Sm, Fe, and Graphite by Mechanical Alloying. *J. Appl. Phys.* **2000**, *87*, 5296–5298. [CrossRef]
28. Kuhrt, C.; kAtter, M.; Wecker, J.; Schnitzke, K.; Schultz, L. Mechanically Alloyed and Gas-phase Carbonated Highly Coercive $Sm_2Fe_{17}C_x$. *Appl. Phys. Lett.* **1992**, *60*, 2029–2031. [CrossRef]
29. Geng, H.; Ji, Y.; Feng, X.; Zhang, J.; Gao, Y.; Yan, Y.; Wang, W.; Su, F.; Du, X. Preparing $Sm_2Fe_{17}C_x$ Compound by High-Energy Ball-Milling Sm-Fe Alloy in Heptane Followed by Annealing, Re-Milling and Re-Annealing. *Mater. Des.* **2016**, *111*, 140–145. [CrossRef]
30. Fang, Q.; An, X.; Wang, F.; Li, Y.; Du, J.; Xia, W.; Yan, A.; Liu, J.P.; Zhang, J. The Structure and Magnetic Properties of Sm–Fe–N Powders Prepared by Ball Milling at Low Temperature. *J. Magn. Magn. Mater.* **2016**, *410*, 116–122. [CrossRef]
31. Sato, S.; Nishikawa, K.; Node, E.; Okada, S. Development of $TbCu_7$-Type Sm-Fe-N Anisotropic Magnet Powder and Its Sintered Magnets. *J. Alloys Compd.* **2022**, *929*, 167280. [CrossRef]
32. Nakamura, H.; Kurihara, K.; Tatsuki, T.; Sugimoto, S.; Okada, M.; Homma, M. Phase Changes and Magnetic Properties of $Sm_2Fe_{17}N_x$ Alloys Heat-Treated in Hydrogen. *IEEE Transl. J. Magn. Jpn.* **1992**, *7*, 798–804. [CrossRef]
33. Okada, S.; Node, E.; Takagi, K.; Hashimoto, R. Synthesis of Ultra-High Coercivity $Sm_2Fe_{17}N_3$ Powder by Homogeneous Reduction-Diffusion with Rotary Furnace. *J. Alloys Compd.* **2023**, *960*, 170726. [CrossRef]
34. Mao, O.; Altounian, Z.; Yang, J.; Ström-Olsen, J.O. Thermal Stability of Nanostructured Sm2Fe17Cx Compounds Prepared by Ball Milling. *J. Appl. Phys.* **1996**, *79*, 5536–5538. [CrossRef]
35. Shen, B.; Kong, L.; Wang, F.; Cao, L. Structure and Magnetic Properties of $Sm_2Fe_{14}Ga_3C_x$ (X=0–2.5) Compounds Prepared by Arc Melting. *Appl. Phys. Lett.* **1993**, *63*, 2288–2290. [CrossRef]

36. Cao, L.; Müller, K.; Handstein, A.; Grünberger, W.; Neu, V.; Schultz, L. High Performance Permanent Magnets Made by Mechanical Alloying and Hot Pressing. *J. Phys. D Appl. Phys.* **1996**, *29*, 271. [CrossRef]
37. Cheng, Z.; Shen, B.; Zhang, J.; Gong, H.; Zhao, J. The Formation and Magnetic Properties of $Sm_2Fe_{15}Al_2C_x$ (X=0-2.0) Compounds Prepared by Arc Melting. *J. Phys. Condens. Matter* **1994**, *6*, L185. [CrossRef]
38. Cheng, Z.; Shen, B.; Zhang, J.; Wang, F.; Gong, H.; Liang, B.; Zhan, W. Effect of Al on the Formation and Magnetic Properties of $Sm_2Fe_{17}C_x$ (x = 0–2.5) Prepared by Arc-Melting. *J. Magn. Magn. Mater.* **1995**, *140–144*, 1075–1076. [CrossRef]
39. Shelekhov, E.V.; Sviridova, T.A. Programs for X-Ray Analysis of Polycrystals. *Met. Sci. Heat Treat.* **2000**, *42*, 309–313. [CrossRef]
40. Shchetinin, I.V.; Bordyuzhin, I.G.; Sundeev, R.V.; Menushenkov, V.P.; kAmynin, A.V.; Verbetsky, V.N.; Savchenko, A.G. Structure and Magnetic Properties of $Sm_2Fe_{17}N_x$ Alloys after Severe Plastic Deformation by High Pressure Torsion. *Mater. Lett.* **2020**, *274*, 127993. [CrossRef]
41. Hu, B.; Li, H.; Sun, H.; Coey, J.M.D. A ^{5}e Mossbauer Study of a New Series of Rare-Earth Iron Nitrides: $R_2Fe_{17}N_{3\text{-delta}}$. *J. Phys. Condens. Matter.* **1991**, *3*, 3983. [CrossRef]
42. Fujii, H.; Sun, H. *Handbook of Magnetic Materials*; Buschow, K.H.J., Ed.; Elsevier: Amsterdam, The Netherlands, 1995; Volume 9, pp. 341–345.
43. Bessais, L. Structure and Magnetic Properties of Intermetallic Rare-Earth-Transition-Metal Compounds: A Review. *Materials* **2022**, *15*, 201. [CrossRef]
44. Qi, Q.; Sun, H.; Coey, J.M.D. Mössbauer Studies of Interstitial Rare Earth-Iron Intermetallics. *Hyperfine Interact.* **1992**, *68*, 27–38. [CrossRef]
45. Wang, Y.Z.; Hadjipanayis, G.C. Magnetic Properties of $Sm_2Fe_{17}C_x$ Compounds. *J. Appl. Phys.* **1991**, *69*, 5565–5567. [CrossRef]
46. Hosokawa, A.; Suzuki, K.; Yamaguchi, W.; Takagi, K. Mechanism of Anomalous α-Fe Formation from Stoichiometric Sm_2Fe_{17} Jet-Milled Powder during Post-Pulverization Annealing. *Acta Mater.* **2021**, *213*, 116981. [CrossRef]
47. Kumar, A.; Pandel, U.; Banerjee, M.K. Effect of High Energy Ball Milling on the Structure of Iron—Multiwall Carbon Nanotubes (MWCNT) Composite. *Adv. Mater. Res.* **2017**, *6*, 245–255. [CrossRef]
48. Liu, X.-W.; Zhao, S.; Meng, Y.; Peng, Q.; Dearden, A.K.; Huo, C.-F.; Yang, Y.; Li, Y.-W.; Wen, X.-D. Mössbauer Spectroscopy of Iron Carbides: From Prediction to Experimental Confirmation. *Sci. Rep.* **2016**, *6*, 26184. [CrossRef]
49. Nikolenko, P.I.; Nizamov, T.R.; Bordyuzhin, I.G.; Abakumov, M.A.; Baranova, Y.A.; Kovalev, A.D.; Shchetinin, I.V. Structure and Magnetic Properties of $SrFe_{12-x}In_xO_{19}$ Compounds for Magnetic Hyperthermia Applications. *Materials* **2023**, *16*, 347. [CrossRef]